The Structure of Nitric Oxide Synthase Oxygenase Domain and Inhibitor Complexes

Brian R. Crane,* Andrew S. Arvai, Ratan Gachhui, Chaoqun Wu, Dipak K. Ghosh, Elizabeth D. Getzoff, Dennis J. Stuehr,† John A. Tainer†

The nitric oxide synthase oxygenase domain (NOS_{ox}) oxidizes arginine to synthesize the cellular signal and defensive cytotoxin nitric oxide (NO). Crystal structures determined for cytokine-inducible NOS_{ox} reveal an unusual fold and heme environment for stabilization of activated oxygen intermediates key for catalysis. A winged β sheet engenders a curved α-β domain resembling a baseball catcher's mitt with heme clasped in the palm. The location of exposed hydrophobic residues and the results of mutational analysis place the dimer interface adjacent to the heme-binding pocket. Juxtaposed hydrophobic O_2- and polar L-arginine–binding sites occupied by imidazole and aminoguanidine, respectively, provide a template for designing dual-function inhibitors and imply substrate-assisted catalysis.

Nitric oxide is a reactive, gaseous, lipophilic molecule that functions at high concentrations as a defensive cytotoxin against tumor cells and pathogens, and at low concentrations as a signal in many diverse physiological processes including blood flow regulation, neurotransmission, learning, and memory (*1*, *2*). Nitric oxide is notable among signals for its rapid diffusion, ability to permeate cell membranes, and intrinsic instability, properties that eliminate the need for extracellular NO receptors or targeted NO degradation. Nitric oxide synthases (NOSs), expressed as cytokine-inducible (iNOS), endothelial (eNOS), and neuronal (nNOS) isozymes, oxidize L-arginine (L-Arg) to NO and citrulline, thereby controlling NO distribution and concentrations in higher eukaryotes (*1*, *2*).

The iNOS isozyme is critical for the immune response, but it is also implicated in most diseases involving NO overproduction. Constitutive eNOS and nNOS generate NO that is imperative for blood circulation and signal transmission in the nervous system (*1*). Pathologies linked to excessive NO production include immune-type diabetes, inflammatory bowel disease, rheumatoid arthritis, carcinogenesis, septic shock, multiple sclerosis, transplant rejection, and stroke, and pathologies linked to insufficient NO production include hypertension, impotence, arteriosclerosis, and susceptibility to infection (*1*–*3*). Isozyme-specific inhibitors of NOS, particularly of iNOS, are desirable both for medicinal purposes and to advance our understanding of basic physiology (*3*).

NOS generates NO from a two-step, heme-based oxidation of L-Arg that forms N^{ω}-hydroxy-L-arginine (NOH-L-Arg) as a stable intermediate (*2*, *4*, *5*). The first step likely involves a mixed-function oxidation similar to those catalyzed by the cytochrome P-450s: L-Arg + O_2 + NADPH + H^+ ↔ NOH-L-Arg + H_2O + $NADP^+$ (*6*, *7*). Further oxidation of NOH-L-Arg may proceed by an unusual mechanism where one electron from NADPH [the reduced form of nicotinamide adenine dinucleotide phosphate ($NADP^+$)], one electron from NOH-L-Arg, and O_2 form a dioxygen-iron species that attacks the guanidino carbon of the resulting NOH-L-Arg radical, leading to oxygen incorporation and C-N bond scission: NOH-L-Arg + O_2 + 1/2 (NADPH + H^+) ↔ L-citrulline + NO + H_2O + 1/2 $NADP^+$ (*2*, *8*).

NOS isozymes differ in size (130 to 160 kD), amino acid sequence (50 to 60% identity between any two isozymes), tissue distribution, transcriptional regulation, and activation by intracellular calcium (*1*), but they share an overall three-component construction (*1*, *2*, *4*, *5*): (i) an NH_2-terminal catalytic oxygenase domain (NOS_{ox}, residues 1 to 498 for iNOS) that binds heme (iron protoporphyrin IX), tetrahydrobiopterin (H_4B), and the substrate L-Arg; (ii) a COOH-terminal reductase domain (NOS_{red}, residues 531 to 1144 for iNOS) that binds flavin mononucleotide (FMN), flavin adenine dinucleotide (FAD), and NADPH; and (iii) an intervening calmodulin-binding region (residues 499 to 530 for iNOS) that regulates electronic communication between NOS_{ox} and NOS_{red} (*5*, *9*). Dimerization of NOS_{ox}, promoted by L-Arg and H_4B, is necessary for catalytic activity in vitro (*2*, *4*, *5*, *9*) and may regulate activity in vivo (*9*). Although NH_2-terminal truncation of $iNOS_{ox}$ after residue 114 attenuates dimerization (*10*), some catalytic activity is retained (*11*). Analogously truncated eNOS that includes NOS_{red} binds L-Arg and H_4B and retains up to 12% of native activity (*12*).

Structure determination and domain fold of $iNOS_{ox}$. Structures from orthorhombic crystals (*13*) containing one molecule per asymmetric unit of $iNOS_{ox}$ Δ114 (residues 115 through 498 plus a COOH-terminal tag of six histidines for affinity purification) in complex with imidazole (Table 1, $P2_12_12_1$-IM) and with aminoguanidine and imidazole (Table 1, $P2_12_12_1$-AG) were determined to 2.1 and 2.3 Å resolution, respectively, by multiple isomorphous replacement (Table 1) (*14*, *15*). We resolved discontinuities in the polypeptide chain arising from weak electron density for projecting loop regions in the orthorhombic crystal form (residues 328 to 335, 383 to 401, and 446 to 477) by also determining a 2.6 Å resolution $iNOS_{ox}$ Δ114 structure from a $P2_13$ cubic crystal form obtained by cocrystallization with *Escherichia coli* type I chloramphenicol acetyltransferase (CAT) (Table 1, $P2_13$-IM) (*16*). The cubic lattice packing enforced by the CAT trimer stabilized the projecting loop regions, leaving only one disordered surface loop (residues 449 to 457) in an otherwise nearly identical $iNOS_{ox}$ structure.

The $iNOS_{ox}$ Δ114 structure reveals an elongated, curved molecule (80 Å by 57 Å by 30 Å) with an unusual nonmodular, single-domain α-β fold that resembles a baseball catcher's mitt for the left hand (Figs. 1 to 3). Heme is clasped in the mitt's webbed β sheet palm with its distal face directed toward a large exposed cavity (~20 Å across and ~11 Å deep) where two imidazole molecules are found in both crystal forms (Fig. 1A). The fold's dominant feature is a winged β sheet, with projecting β hairpins and flanking α helices (Fig. 1A). Three long, antiparallel β strands (β4, β8, and β9), each composed of three segments (labeled a, b, and c), zigzag across the length of the β structure (Fig. 1B). The middle segments and two preceding parallel β strands form the main five-stranded mixed

B. R. Crane, A. S. Arvai, E. D. Getzoff, and J. A. Tainer are in the Department of Molecular Biology and the Skaggs Institute for Chemical Biology, The Scripps Research Institute, La Jolla, CA 92037, USA. R. Gachhui, C. Wu, D. K. Ghosh, and D. J. Stuehr are in the Department of Immunology, Cleveland Clinic, Cleveland, OH 44106, USA.

*Present address: Beckman Institute, California Institute of Technology, Pasadena, CA 91125, USA.
†To whom correspondence should be addressed.

β sheet, whereas the end segments participate in four- and six-stranded β wings, each roughly perpendicular to the main β sheet and coplanar with each other (Fig. 1). Two α-β rolls mount α3 and α4, respectively, under each wing and alongside the main sheet, whereas a third α-β roll wraps α5 with β4c and β6a from the six-stranded wing. The conformational uniqueness of conserved Pro and Gly residues (Fig. 2) and specific side-chain to main-chain hydrogen bonds allow for the extensive hydrogen bond switching between zigzagged β strand pairs that is needed for wing formation. Long helical hairpins cap both ends of the winged β sheet, and a fifth long helix runs lengthwise between these hairpins (Fig. 1). The $iNOS_{ox}$ polypeptide topology was not detected among other known protein structures by the similarity search program Dali (*17*); however, the high sequence conservation of many key structural and active-site residues among the three NOS isoforms (Fig. 2) indicates that eNOS and nNOS share the unusual $iNOS_{ox}$ fold.

The NOS heme environment. The NOS distal heme pocket, primarily constructed from β structure, differs considerably from the distal pockets of heme-based oxygenases, oxidases, peroxidases, and catalases, which are largely α-helical [survey of the Protein Data Bank (PDB) (*18*)]. In these $iNOS_{ox}$ structures, the low-spin ferric heme iron is axially coordinated to proximal Cys^{194} (2.3 Å bond), consistent with mutagenesis and spectroscopic data (*19–22*), and to exogenous imidazole (2.0 Å bond) (Figs. 1A and 4). Most proximal interactions with the heme involve the α3-β2 loop containing Cys^{194}, whereas the hydrophobic distal pocket is formed by residues from the main β sheet (β8b and β9b), β9c, and the four-stranded wing (β8c) (Fig. 1). An arc of conserved hydrophobic residues (Phe^{363}, Val^{346}, Pro^{344}, Tyr^{367}, Ile^{372}, and Met^{368}) curves around the heme coordination site (Figs. 2 and 4). Proximal Trp^{188} and distal Phe^{363} sandwich the porphyrin ring, whereas additional conserved hydrophobic residues (Leu^{203}, Ile^{238}, Trp^{366}, Met^{368}, Met^{428}, Tyr^{483}, and Tyr^{485}) along with Ser^{236} encircle the heme's edge, leaving only the heme carboxylates to extend into solvent (Fig. 4). Differences between the ring D propionate orientations found in the cubic and orthorhombic crystal forms affect heme ruffling and suggest that conformational switching of this pyrrole propionate can occur and may affect heme planarity, dimer formation, or catalysis. Although the immediate distal heme pocket in NOS is largely hydrophobic and devoid of hydrogen-donating groups (Fig. 2, blue boxed), polar residues at the pocket edge (Fig. 2, cyan boxed; Fig. 4) may influence L-Arg or H_4B binding and dimerization. The closest hydrophilic residue to the heme iron, Glu^{371}, hydrogen bonds to the second imidazole and is required for L-Arg binding (*23, 24*), thereby localizing the substrate binding site over heme pyrrole rings A and B (Fig. 4). The high residue identity among the three NOS isozymes within the observed heme environment (Fig. 2; blue and cyan boxed) suggests that differences in activity among isozymes are manifested by sequence variability in the NH_2-terminal region and the dimer and reductase domain interfaces.

The dramatic differences in fold, heme location, and heme environment between $iNOS_{ox}$ and the known cytochrome P-450 structures emphasize that these two enzyme families have achieved similar catalytic ac-

Table 1. Diffraction data and refinement statistics for $iNOS_{ox}$ inhibitor complexes and heavy atom derivatives.

Data set*	Res. (Å)†	R_{sym}‡ (%)	⟨I/σI⟩§	Comp.‖ (%)	Res./*Ph*¶	R_{iso} (%)#	R_{cen} / R_{Kraut}** (%)	PP_{iso} / PP_{ano}††	Sites‡‡
				Inhibitor complexes					
$P2_12_12_1$-IM	2.1 (2.2–2.1)	4.6 (31.8)	28.0 (4.8)	99.7 (100.0)	–	–	–	–	–
$P2_12_12_1$-AG	2.3 (2.4–2.3)	6.8 (31.1)	17.8 (3.9)	99.7 (100.0)	–	–	–	–	–
$P2_13$-IM	2.6 (2.7–2.6)	5.9 (31.0)	30.6 (2.9)	98.9 (92.0)	–	–	–	–	–
				Heavy atom derivatives					
EMP	2.9 (3.0–2.9)	8.6 (33.5)	14.6 (4.7)	98.2 (96.8)	2.9/2.9	18.4	62/28	1.66/2.73	3
OSM	2.7 (2.8–2.7)	8.3 (32.8)	15.1 (4.7)	100 (99.5)	3.0/3.5	20.3	65/30	1.58/1.95	1
OSM-EMP	2.4 (2.5–2.4)	6.3 (31.2)	19.0 (4.1)	99.2 (99.2)	2.8/3.5	36.5	64/24	1.53/2.14	3
PCMB	2.2 (2.3–2.2)	5.9 (34.1)	12.0 (2.3)	50.1 (53.7)	3.0	14.0	68	1.38	2
B-diHg	3.0 (3.1–3.0)	7.6 (38.0)	19.1 (5.0)	89.0 (86.0)	3.1	25.5	68	1.23	4
diHg-F	3.0 (3.1–3.0)	8.5 (32.5)	18.1 (5.7)	95.5 (97.7)	3.5	38.7	67	0.61	4
EMTS	2.5 (2.6–2.5)	7.2 (32.7)	18.7 (4.2)	100 (100)	3.0	20.5	63	0.97	2

Refined structure	Res. (Å)†	R_{cryst}§§	R_{free}‖‖	Total scatterers	Waters	Total observations	Unique reflections	rmsd¶¶ bonds, angles
				Refinement statistics				
$P2_12_12_1$-IM	2.1 (2.2–2.1)	20.5 (29.6)	26.1 (32.5)	2922	255	112,723	25,837	0.007 Å, 1.6°
$P2_12_12_1$-AG	2.3 (2.4–2.3)	20.4 (26.7)	25.1 (25.2)	2873	205	77,851	19,773	0.007 Å, 1.6°
$P2_13$-IM	2.6 (2.7–2.6)	22.1 (32.3)	25.7 (37.8)	4970	140	226,448	32,117	0.007 Å, 1.5°

*Inhibitor complexes and heavy atom derivatives. The $iNOS_{ox}$ inhibitor complexes are listed by space group followed by inhibitor, where IM is the imidazole complex and AG is the aminoguanidine complex. PDB codes are 1nos for $P2_12_12_1$-IM, 2nos for $P2_12_12_1$-AG, and 1noc for $P2_13$-IM. Derivatives of $P2_12_12_1$-IM: EMP—0.2 mM ethylmercury phosphate 50 mM imidazole/molate (IM/M), 75 mM Na_2SO_3, pH 5.0, 12 hours; OSM—0.3 mM K_2OsCl_6, 25 mM Hepes, pH 7.5, 50 hours; OSM-EMP—0.66 mM K_2OsCl_6, 0.2 mM ethylmercury phosphate, 20 mM tris, pH 10.0, 24 hours; PCMB—1 mM *p*-chloromercuribenzoate, 20 mM tris, pH 10.0, 24 hours; B-diHg—10 μM Baker's dimercurial, 50 mM IM/M, 75 mM Na_2SO_3, pH 5.0, 20 hours; diHG-F—100 μM dimercury fluorescein, 20 mM IM/M, 20 mM Na_2SO_3 pH 7.2, 12 hours; EMTS—cocrystallization with 10 mM ethyl mercurithiosalicylate. Residues Cys^{211} and Cys^{222} were the major sites of modification for all compounds, except OSM, which reacted only with Cys^{211}. †Highest resolution of the data set followed in brackets by the range of resolution in the highest resolution bin for compiling statistics. ‡‡$R_{sym} = \Sigma_h\Sigma_j|I_{hj} - \langle I_h\rangle|/\Sigma_h\Sigma_j I_{hj}$, where I_{hj} is the intensity of observation *j* of reflection *h*. §Intensity signal-to-noise ratio. ‖Completeness of the unique diffraction data. ¶Resolution cutoff used in isomorphous heavy atom phasing followed by cutoff used in anomalous phasing. #$R_{iso} = \Sigma\,||F_{ph}| - |F_p||/\Sigma|F_p|$ for isomorphous derivatives, where F_{ph} and F_p are the derivative and native structure factor amplitudes, respectively. **R_{cen} isomorphous $= \Sigma\,||F_{ph}| \pm |F_p| - |F_{hc}||/\Sigma\,||F_{ph}| \pm |F_p||$ for centric reflections of isomorphous derivatives (F_{hc} is the calculated heavy atom structure factor), and R_{Kraut} anomalous $= \Sigma\,||F_{ph}^+| - |F_{phc}^+|| + ||F_{ph}^-| - |F_{phc}^-||/\Sigma|F_{ph}^+| + |F_{ph}^-|$ in the case of anomalous scattering. ††Phasing power for isomorphous derivatives (PP_{iso}) $= \langle|F_{hc}|\rangle/\langle E\rangle$, where *E* is the residual lack of closure error, and phasing power for anomalous derivatives (PP_{ano}) $= \langle 2|F_h''|\rangle/\langle E\rangle$, where F_h'' is the calculated anomalous-scattering structure factor. ‡‡Sites refers to the number of heavy or anomalously scattering centers. §§$R_{cryst} = \Sigma||F_{obs}| - |F_{calc}||/\Sigma|F_{obs}|$ for all reflections (no σ cutoff), where F_{obs} and F_{calc} are the observed and calculated structure factors, respectively. ‖‖R_{free} was calculated against 10% of the reflections removed at random for the orthorhombic data, and 5% removed for the cubic data. ¶¶Root-mean-square deviations (rmsd) from the ideal bond and angle restraints complement excellent stereochemistry and residue packing (*40*).

tivity through convergent evolution (Fig. 5). Despite similarities among NOSs and P-450s in the Arg-Cys-Ile-Gly-Arg sequence flanking the proximal Cys ligand (*25*) (Fig. 5), the charge density on the iNOS proximal Cys[194] thiolate should be reduced by additional hydrogen bonds to the thiolate from the peptide nitrogen at position +3, and the indole nitrogen of Trp[188], along with a Gln-to-Arg replacement at position +3 for hydrogen bonding to the Cys carbonyl. Lower electron density on the cysteine thiolate of iNOS is consistent with increased stretching frequencies of heme-bound CO in NOSs as compared with P-450s (*22*). Chloroperoxidase, an enzyme with both peroxidase and monooxygenation activities (*26*), also has additional hydrogen bonds to its proximal cysteine (PDB code 1cpo) that correlate with a decreased heme-thiolate interaction indicated by vibrational spectroscopy (*22*).

Inhibitor binding and domain interfaces. Two juxtaposed molecules of the NOS inhibitor imidazole occupy the distal pocket in both crystal forms of $iNOS_{ox}$ (Figs. 1A, 4, and 6A), explaining the effects of imidazole on heme spectra, substrate binding, and dimerization. One imidazole (IM1) binds directly to the heme iron as a sixth ligand and resides deep in the distal pocket, making no hydrogen bonds to any protein residues, whereas the second (IM2) resides above the edge of heme pyrrole ring A and hydrogen bonds with Glu[371] (Figs. 4 and 6A). IM1 coordination of the heme iron accounts for the low-spin shift in the heme electronic state caused by imidazole (*27, 28*), whereas IM2 interaction with Glu[371] likely explains competitive inhibition of L-Arg and H_4B binding by imidazole and its ability to promote dimerization (*11, 28*). Van der Waals interactions of Val[346] and Phe[363] with IM1 tilt the ligand 10° from the heme normal toward Glu[371] and IM2 (Fig. 6A). Similar contacts would direct dioxygen species angularly bound to the heme toward Glu[371] and thereby facilitate oxygen-substrate interactions. This unexpected discovery of two distinct, adjacent imidazole binding sites has important implications for drug design. Dual-function inhibitors that simultaneously bind both Glu[371] and the heme would expand the binding region to increase affinity and would block L-Arg and dioxygen binding, preventing formation of toxic, reactive oxygen species at the heme iron. Because the characteristics of NOS inhibition by imidazole vary among isozymes and species (*28*), dual-function inhibitors may also afford isozyme-selective inhibition.

When soaked into the $iNOS_{ox}$ Δ114 crystals at 10 mM, the L-Arg analog and mechanism-based inactivator aminoguanidine (*29*) binds in the distal pocket adjacent to the heme by interacting directly with Glu[371], replacing IM2 (Fig. 6B). Aminoguanidine stacks over a heme meso carbon (CHB) and the edge of pyrrole ring A at an angle ~45° to the heme plane. An aminoguanidine guanidino nitrogen and the amino nitrogen hydrogen bond to a carboxyl oxygen atom of Glu[371], whose constrained side-chain conformation is stabilized by hydrogen bonds from its carboxylate oxygens to its own peptide nitrogen and the peptide nitrogens of and Met[368] and Gly[369] (Fig. 6B). This configuration places both guanidino terminal nitrogens of aminoguanidine within hydrogen-bonding distance of the Trp[366] peptide carbonyl at the pocket's base and directs one terminal guanidino nitrogen toward where heme-bound activated oxygen, implicated in the conversion of L-Arg to NOH-L-Arg, would reside. Such close proximity between the heme iron and a gua-

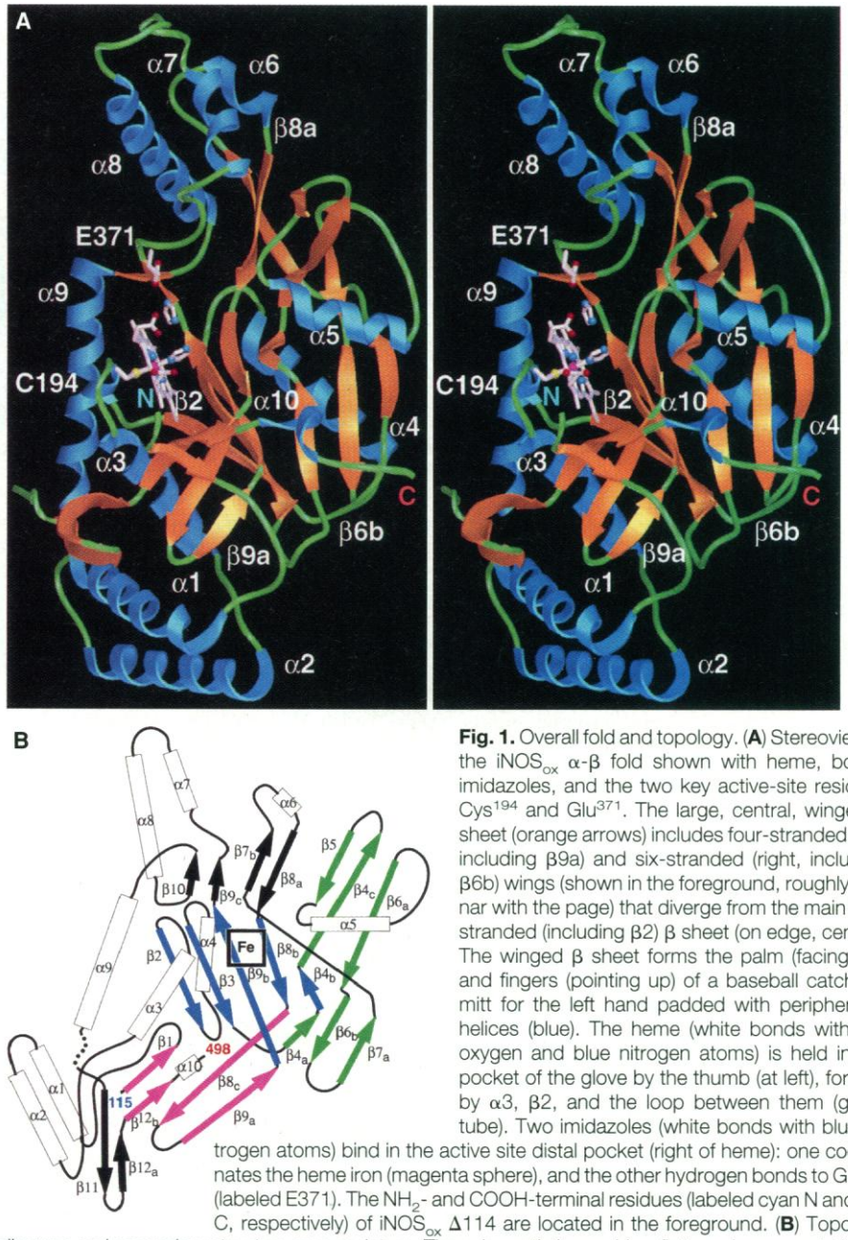

Fig. 1. Overall fold and topology. (**A**) Stereoview of the $iNOS_{ox}$ α-β fold shown with heme, bound imidazoles, and the two key active-site residues Cys[194] and Glu[371]. The large, central, winged β sheet (orange arrows) includes four-stranded (left, including β9a) and six-stranded (right, including β6b) wings (shown in the foreground, roughly planar with the page) that diverge from the main five-stranded (including β2) β sheet (on edge, center). The winged β sheet forms the palm (facing left) and fingers (pointing up) of a baseball catcher's mitt for the left hand padded with peripheral α helices (blue). The heme (white bonds with red oxygen and blue nitrogen atoms) is held in the pocket of the glove by the thumb (at left), formed by α3, β2, and the loop between them (green tube). Two imidazoles (white bonds with blue nitrogen atoms) bind in the active site distal pocket (right of heme): one coordinates the heme iron (magenta sphere), and the other hydrogen bonds to Glu[371] (labeled E371). The NH_2- and COOH-terminal residues (labeled cyan N and red C, respectively) of $iNOS_{ox}$ Δ114 are located in the foreground. (**B**) Topology diagram and secondary structure nomenclature. The schematic is roughly a flattened representation of (A). In the winged β sheet, many β strands (arrows) switch hydrogen-bonding partners to participate in more than one of the component β structures: main five-stranded β sheet (blue), four-stranded wing (magenta), six-stranded wing (green), and projecting β strand pairs (black). The heme (open square with central Fe) packs against the main sheet. The flanking α helices (white boxes) lie predominantly along one side (left) of this single-domain fold. Residues 449 to 457 (dotted line) are disordered in both the cubic and orthorhombic crystal forms.

nidino nitrogen is consistent with models for NOS catalysis (*2*, *4*, *8*) and may explain how various L-Arg analogs can differentially affect the electronic properties of the heme iron (*20*) as well as the vibrational frequencies and stability of heme ligands such as NO, CO, and O_2 bound in the NOS active center (*22*, *30*, *31*). Superimposing the guanidinum group of L-Arg on that of NOS-bound aminoguanidine (so as to avoid unrealistically close contacts with the protein) orients the L-Arg aliphatic side chain toward the proposed dimer interface at the edge of the distal pocket (see below), placing the amino acid group near Gln^{257}, Arg^{260}, Tyr^{367} (Figs. 4 and 6B), and Tyr^{341} (*32*). A similar location of L-Arg in the active site of dimeric iNOS would position a terminal guanidino nitrogen close enough to the heme iron to interact directly with iron-bound oxygen species and would also spatially permit hydroxylation of this terminal nitrogen. These structural results, coupled with the observation that the reduction of one heme is sufficient to drive NO synthesis in an intact $iNOS_{ox}$ dimer (9), indicate that the two active centers in dimeric NOS likely function independently of one another.

The location of the second imidazole at the edge of the open distal heme pocket in the cupped palm of $iNOS_{ox}$ Δ114, together with the distribution of exposed conserved hydrophobic residues, highly mobile regions, and dimer-destabilizing mutations on the exposed surface, all suggest the same mode for NOS dimer assembly. The isozyme-conserved, exposed, hydrophobic surface area of $iNOS_{ox}$ Δ114 (Figs. 2 and 3) is unusually large—over twice that found in cytochrome $P\text{-}450_{cam}$ (PDB code 2cpp), a soluble monooxygenase of similar size but different structure (*32*). More than 90% of this conserved hydrophobic surface area maps adjacent to the concave face of $iNOS_{ox}$ that includes the distal heme pocket (Fig. 3). Regions of $iNOS_{ox}$ Δ114 with the highest crystallographic thermal factors (α9 and the β7b-α6, α7-α8, α9-β11, and β11-β12 loops) and mutation sites that inhibit dimer formation, H_4B binding, and substrate binding (Figs. 2 and 3A) cluster on this same face. Subunit dimerization in conjunction with H_4B or L-Arg binding likely stabilizes and possibly conformationally alters these mobile regions and the flexible, missing NH_2-terminus. The open distal pocket in the NOS_{ox} subunit contrasts with the buried distal heme pockets of the cyto-

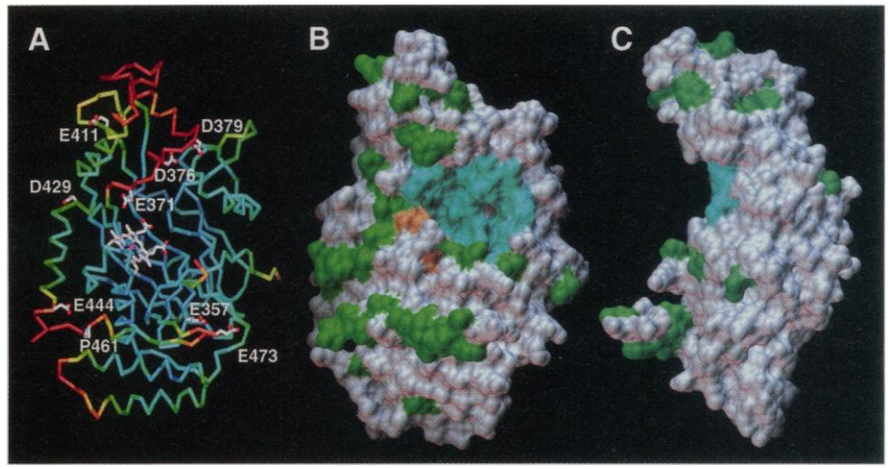

Fig. 3. Mobility, surface properties, and shape. (**A**) Cα trace of NOS_{ox} Δ114 (cubic crystal form) colored by the crystallographic temperature factor (low to high *B* factors colored blue to red) and displayed with heme and mutation sites that affect function. Mutation sites (side chains displayed and labeled by residue number) affecting dimerization, L-Arg binding, or H_4B binding (defined in Fig. 2) cluster to highly mobile (red) projecting regions. The view is rotated by about 45° from Fig. 1 about a vertical axis. (**B**) Solvent-accessible molecular surface of flattened (left) and concave (center) face. The orientation is the same as in (A). The exposed heme edge (gold), residues contributing to the distal pocket (cyan), and exposed conserved hydrophobic residues (green) (defined in Fig. 2) map to the same flattened face of the molecule and cluster in the regions of high mobility and mutational sensitivity shown in (A), making this surface the prime candidate for a symmetric dimer interface. (**C**) Solvent-accessible molecular surface of the narrow curved face. This face has few conserved exposed hydrophobic residues. The view is rotated 90° from (A) and (B) around a vertical axis.

Fig. 2. Residue function, secondary structure, and sequence conservation. Sequence alignment of murine $iNOS_{ox}$ (GenBank accession number M84373), bovine $eNOS_{ox}$ (M89952), and human $nNOS_{ox}$ (U17327), highlighting the proximal heme ligand Cys^{194} and substrate-binding residue Glu^{371} (yellow background), exposed conserved hydrophobic residues (green background), mutation sites affecting function (red letters), and residues bordering the heme site (boxed) on the proximal side and edge (magenta) and in the immediate (blue) and extended (cyan) distal pocket (Fig. 3, B and C). Exposed, conserved, hydrophobic positions have Ala, Cys, Leu, Met, Phe, Pro, Trp, Tyr, or Val in all three sequences and more than 50 $Å^2$ of carbon or sulfur molecular surface area exposed to a solvent probe sphere of radius 1.4 Å. Mutations in $iNOS_{ox}$ residues 371, 376, 379, 429, 444, and 473 affect L-Arg binding; 379, 429, 444, 454, and 473 affect H_4B binding; and 411, 450, 452, 453, and 461 affect dimerization or activity (*11*, *24*). Mutation at $eNOS_{ox}$ residue 349 (357 iNOS) also affects activity (*23*). Above the sequences, black arrows show β strands, white boxes show α helices, and dotted lines show disordered residues. Below the sequences, solid diamonds mark every tenth position. Single-letter abbreviations for the amino acid residues are as follows: A, Ala; C, Cys; D, Asp; E, Glu; F, Phe; G, Gly; H, His; I, Ile; K, Lys; L, Leu; M, Met; N, Asn; P, Pro; Q, Gln; R, Arg; S, Ser; T, Thr; V, Val; W, Trp; and Y, Tyr.

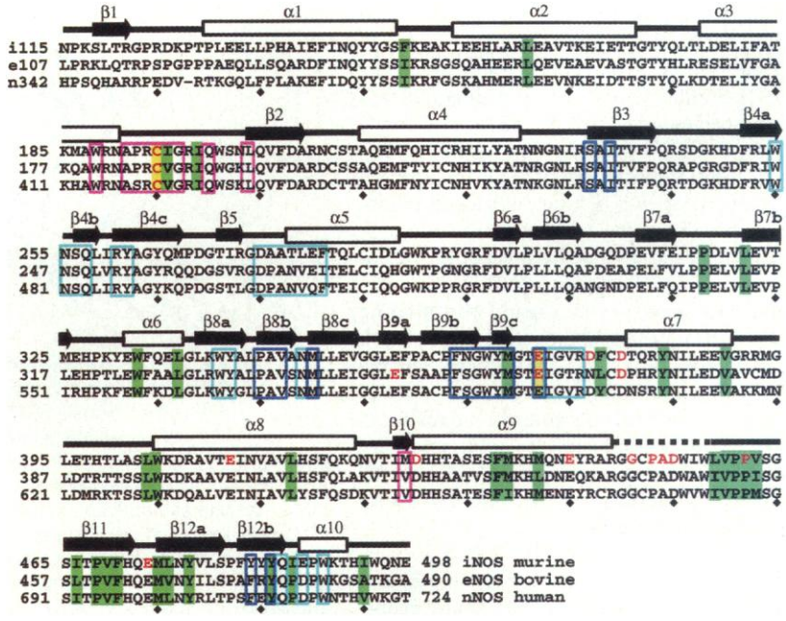

chromes P-450, which are sequestered within the protein core to exclude bulk solvent and thereby control the heme redox potential, production of heme-bound activated oxygen, and catalysis (*6*, *7*, *33*). A primary function of NOS dimerization, manifested by a twofold symmetric association that buries and orders these exposed, hydrophobic, and mobile regions, is to confer stability and reduce solvent exposure of the distal heme pocket, thereby allowing the oxygen activation needed for catalysis. Assuming that dimerization sequesters the heme environment as described above, the remaining exposed, conserved hydrophobic residues (including Phe[148], Ile[198], Leu[321], and Met[368]) (Fig. 2) located on the opposing convex $iNOS_{ox}$ surface formed by β2, α4, β9, and β10 may interface with the FMN-binding region of $iNOS_{red}$, which is likely to be suitably concave by structural analogy to cytochrome P-450 reductase (*34*). This would allow electron transfer from $iNOS_{red}$ to the heme edge that is adjacent to Trp[366] and 6 Å from the surface (Figs. 4 and 6B).

Implications for catalysis and regulation. Comparing $iNOS_{ox}$ structures with other hemoprotein monooxygenase and peroxidase structures identifies special features that may enable function as an NO synthase. As in the cytochrome P-450s, oxygen activation by NOS probably generates discrete intermediates:

$$\text{P-Fe(III)} + e^- + O_2 \rightarrow \text{P-Fe(III)-}O_2^- \xrightarrow{e^-}$$

$$\text{P-Fe(III)-}O_2^{2-} \xrightarrow{2H^+} \text{P}^{\cdot}\text{-Fe(IV)=O} + H_2O$$

In analogy to P-450 monooxygenations (*6*, *7*), NOS also likely uses hypervalent oxo-iron (P·-Fe(IV)=O, where P· is a porphyrin π-cation radical) to hydroxylate L-Arg to NOH-L-Arg in the first step of NO synthesis. However, in the second step, peroxo-iron [P-Fe(III)-O_2^{2-}], formed from the one-electron reduction of superoxide-iron [P-Fe(III)-O_2^-] by NOH-L-Arg, may act to convert the NOH-L-Arg radical to NO and citrulline (*2*, *4*, *8*). In P-450s, the coordination of an electronegative thiolate to the heme iron and the presence of water- or protein-based proton donors are thought to promote generation of oxo-iron from peroxo-iron (*6*, *7*). In contrast, the NOS_{ox} structure may stabilize peroxo-iron relative to oxo-iron by extensive hydrogen bonding to diminish the electronegativity of the heme thiolate ligand, and by the absence in the distal heme pocket of structured water molecules or protein residues that could otherwise donate protons to facilitate scission of the peroxo-iron O–O bond. Indeed, mutations that remove proton-donating residues from the distal pocket of some P-450s increase the proportion of oxidation reactions that proceed through peroxo- rather than oxo-iron (*35*). Because attenuated O–O bond cleaving activity is required for the second step of NO synthesis, NOS may need additional structural features, absent in the P-450s, to facilitate oxo-iron formation in the first step of the reaction. For example, Trp[188] and Phe[363] stack with the heme in $iNOS_{ox}$, a feature important for influencing the electronic and catalytic properties of peroxidases, including formation of oxo-iron porphyrin π-cation radical species [P·-Fe=O(IV)] (*36*). This aromatic stacking may provide quadrupole interactions or resonance delocalization to stabilize the porphyrin π-cation radical of a NOS oxo-iron species.

The aminoguanidine geometry in the $iNOS_{ox}$ active center suggests that substrate-assisted oxygen activation acts in NO synthesis. Heme peroxidases contain a catalytically key, conserved, distal Arg (Arg[44] in cytochrome c peroxidase) that stacks over the heme's edge and directs its N^{ε} toward the heme iron with a configuration similar to the terminal aminoguanidine nitrogen in the $iNOS_{ox}$-aminoguanidine

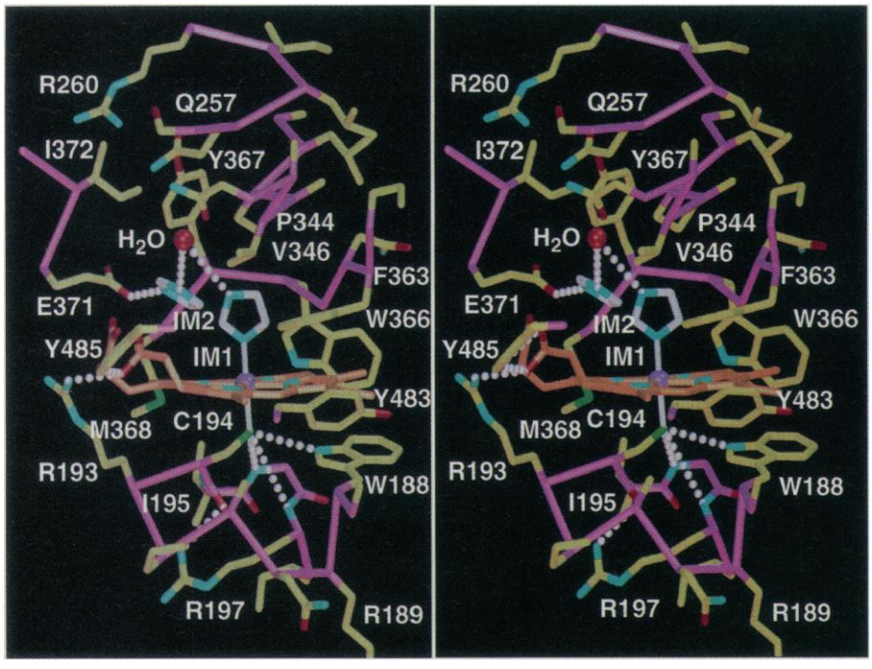

Fig. 4. The heme environment. Stereoview shows distal pocket (above) and proximal heme environment (below) in the cubic crystal form, with the Cα trace colored magenta and side chains in yellow with red oxygen, blue nitrogen, and green sulfur atoms. Two imidazole molecules (white) bind in the distal pocket: IM1 coordinates directly to the heme (gold, with magenta iron), whereas IM2 hydrogen bonds to Glu[371] (E371), and both hydrogen bond to a water molecule (red sphere) at the edge of the pocket. On the proximal heme side, hydrogen bonds (white dots) from the indole nitrogen of Trp[188] (W188), which stacks with the heme plane, and the peptide nitrogens of Gly[196] and Arg[197] (R197) stabilize the charge and conformation of the proximal cysteine thiolate heme ligand Cys[194] (C194). To the left Arg[193] (R193) hydrogen bonds with the heme ring C carboxylate and shields the heme edge from solvent.

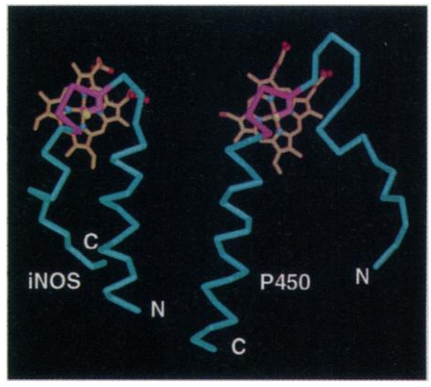

Fig. 5. Comparison of the proximal heme-binding regions of $iNOS_{ox}$ and cytochrome P450s. Structural elements contributing to the proximal heme-binding regions of $iNOS_{ox}$ Δ114 and $P450_{cam}$ (cyan Cα traces) are substantially different. Only the proximal Cys ligands (magenta bonds with yellow sulfur atoms, bound to gold hemes) and immediately COOH-terminal three residues (magenta Cα traces) have similar conformations. In $iNOS_{ox}$, Cys[194] lies at the COOH-terminal end of a helix and precedes an extended strand, whereas in $P450_{cam}$, Cys[357] lies at the NH_2-terminal end of a helix and follows an extended strand. Also, these two cysteine thiolates bind opposite faces of iron protoporphyrin IX. Cα positions for $iNOS_{ox}$ Δ114 residues 194 to 197 were superimposed with $P450_{cam}$ residues 357 to 360 and then separated for clarity.

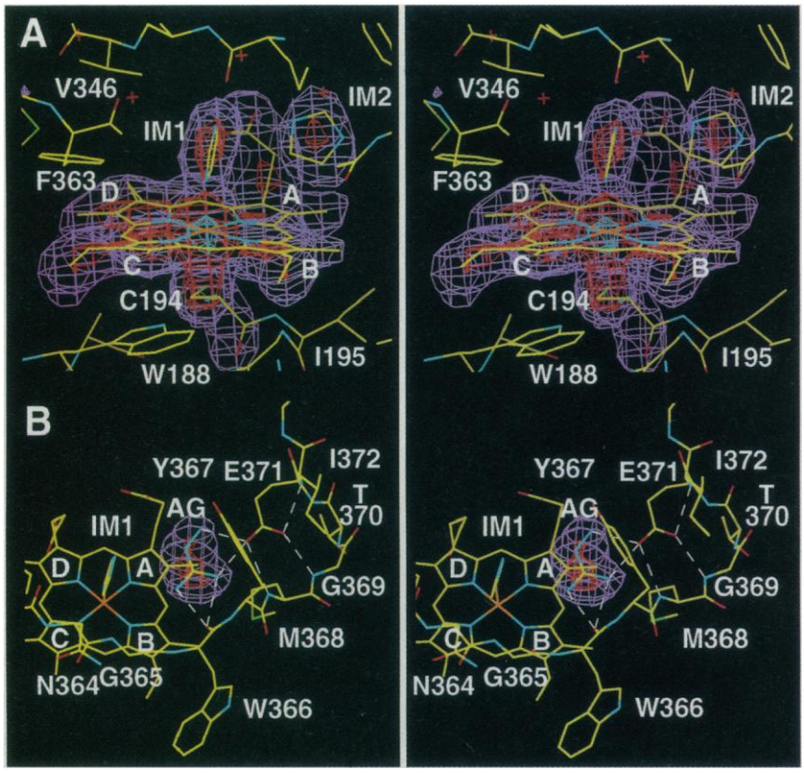

Fig. 6. Inhibitor binding within the distal pocket. (**A**) The 2.1 Å resolution refined model (yellow carbon, red oxygen, blue nitrogen, and green sulfur bonds) and $F_{obs} - F_{calc}$ omit electron density map (purple, 3.5σ, red, 8σ, and cyan, 20σ basket-weave contours), calculated without the heme, Cys[194], or the imidazoles contributing to F_{calc}, for the $iNOS_{ox}$ Δ114-IM complex in the orthorhombic crystal form. Two adjacent imidazoles (IM1 and IM2) bind in the distal pocket. The heme-bound imidazole (IM1) is inclined from the heme normal by 10° because of van der Waals contacts (upper left) with Val[346] (V346) and Phe[363] (F363). (**B**) The 2.3 Å resolution refined model (yellow carbon, red oxygen, blue nitrogen, and green sulfur bonds) and $F_{obs} - F_{calc}$ omit electron density map (purple, 3.5σ and red, 7.5σ basket-weave contours) for aminoguanidine complexed with $iNOS_{ox}$ Δ114. Aminoguanidine (AG) binds alongside the heme-bound imidazole (IM1) above pyrrole ring A and hydrogen bonds (dashed white lines) with both guanidino terminal nitrogens to the main-chain carbonyl oxygen of Trp[366] (W366), and with terminal amino and guanidino nitrogens to the Glu[371] (E371) carboxylate. The other terminal guanidino nitrogen is directed toward the heme distal axial coordination position, where activated oxygen is created for L-Arg hydroxylation.

complex (Fig. 6B). The importance of this Arg for forming oxo-iron in peroxidases (*37*) suggests that L-Arg in NOS supplies hydrogen-bonding interactions to help generate the oxo-iron intermediate needed for its own conversion to NOH-L-Arg.

The unusual fold, structure, and assembly of NOS_{ox} are well adapted for the catalytic and regulatory requirements of NO. The NOS_{ox} winged β sheet and elongated structure place the heme and L-Arg binding site near the protein surface and proposed dimer interface, orient the L-Arg charged amino acid group for interaction with the other subunit or pterin at the pocket's exposed hydrophilic rim, and project the L-Arg guanidinium group toward the heme iron for interaction with activated oxygen in a hydrophobic environment. An active center created by an interface allows substrate and effector molecules such as H_4B and calmodulin to modulate catalysis by affecting associations between domains and subunits. Although NO synthesis by the one-electron reduction of nitrite, as catalyzed by many prokaryotic dissimilatory nitrite reductases (*38*), is far simpler than by the complicated oxidation of L-Arg catalyzed by multimeric NOSs, it is less conducive to regulation. Thus, NO may have evolved to be an effective signal in higher organisms not only because of its unique chemical properties, but also because of the regulatory opportunities provided by its synthesis from L-Arg by NOS.

REFERENCES AND NOTES

1. S. Moncada and A. Higgs, *N. Eng. J. Med.* **329**, 2002 (1993); C. Nathan and Q. Xie, *Cell* **78**, 915 (1994); H. H. Schmidt and U. Walter, *ibid.*, p. 919.
2. O. W. Griffith and D. J. Stuehr, *Annu. Rev. Physiol.* **57**, 707 (1995).
3. G. J. Southan and C. Szabo, *Biochem. Pharmacol.* **51**, 383 (1996).
4. B. Mayer and E. R. Werner, *Nauyn-Schmiedebergs Arch. Pharmacol.* **351**, 453 (1995).
5. B. S. S. Masters *et al.*, *FASEB J.* **10**, 552 (1996).
6. E. J. Mueller, P. J. Loida, S. G. Sligar, in *Cytochrome P450: Structure, Mechanism, and Biochemistry*, P. R. Ortiz de Montellano, Ed. (Plenum, New York, 1995), pp. 83–124.
7. M. Sono, M. P. Roach, E. D. Coulter, J. H. Dawson, *Chem. Rev.* **96**, 2841 (1996).
8. M. Marletta, *Cell* **78**, 927 (1994).
9. D. Stuehr, *Annu. Rev. Pharmacol. Toxicol.* **18**, 707 (1997).
10. D. K. Ghosh *et al.*, *Biochemistry* **36**, 10609 (1997).
11. D. K. Ghosh, R. Gachhui, C. Wu, N. Sennequier, H. M. Abu-Soud, D. J. Stuehr, unpublished results.
12. I. Rodriguez-Crespo, P. Moënne-Loccoz, T. M. Loehr, P. R. Ortiz de Montellano, *Biochemistry* **36**, 8530 (1997).
13. Crystallization trials with dimeric, full-length murine $iNOS_{ox}$ identified a favored truncation product, with the NH_2-terminal 114 residues removed, conducive to crystal growth under select conditions. Inducible NOS_{ox} Δ114 (including a fused COOH-terminal His_6 tag) was overexpressed in *E. coli* and purified by Ni-chelate chromatography as described previously (*10, 39*). Orthorhombic $iNOS_{ox}$ Δ114 crystals of space group $P2_12_12_1$ (cell dimensions 63.0 Å by 73.8 Å by 92.8 Å, one molecule per asymmetric unit, Matthews coefficient V_M = 2.3 Å^3/dalton, solvent content = 48%) were grown at 32°C from drops containing $iNOS_{ox}$ Δ114 (10 mg/ml), 20 mM Hepes, pH 7.6, 50 mM imidazole/malate (IM/M), pH 5.0, 2.5% saturated Na_2SO_3, 5% glycerol, 0.5 mM dithiothreitol (DTT), and 8% PEG MW 4000 (polyethylene glycol of molecular weight 4000) (final pH of 6.5) by vapor diffusion against reservoir containing 100 mM IM/M, pH 5.0, 5% saturated Na_2SO_3, and 16% PEG MW 4000. Cubic crystals (space group $P2_13$, cell dimension of 147.5 Å, V_M = 3.8 Å^3/dalton, solvent content = 68%) of an $iNOS_{ox}$ Δ114–*E. coli* K-12 type I CAT 1:1 complex, obtained by bimolecular crystallization, were grown at 22°C from drops containing $iNOS_{ox}$ Δ114 (10 mg/ml), CAT (~5 mg/ml), 20 mM Hepes, pH 7.6, 5% glycerol, 0.5 mM DTT, 50 mM IM/M, pH 5.0, 27.5% saturated Na_2SO_4 (final pH of 6.5) by vapor diffusion against reservoir containing 100 mM IM/M, pH 5.0 and 55% saturated Na_2SO_4. The aminoguanidine complex was formed by soaking an orthorhombic $iNOS_{ox}$ Δ114 crystal in 10 mM aminoguanidine carbonate, 40 mM Hepes, pH 7.9, and 12% PEG MW 6000 for 30 hours.
14. All native and derivative diffraction data (Table 1) were collected at the Stanford Synchrotron Radiation Laboratory (SSRL) on beam lines 7–1 and 9–1 at −170°C, because weak diffraction of $iNOS_{ox}$ Δ114 precluded data collection from rotating anode x-ray sources. Efficient derivative screening at SSRL allowed extensive exploration of heavy atom concentration, buffer conditions, pH, and soaking times for optimizing orthorhombic $iNOS_{ox}$ Δ114 heavy atom derivatives (Table 1). After data reduction with DENZO [Z. Otwinowski and W. Minor, *Methods Enzymol.* **276**, 307 (1997)], heavy atom positions were found with Patterson techniques, confirmed by cross-Fourier maps calculated in XtalView (*40*), and then optimized by origin-removed Patterson refinement in HEAVY [T. C. Terwilliger and D. Eisenberg, *Acta Crystallogr.* **A39**, 813 (1983)]. Structure factor phases to 2.8 Å resolution, calculated from isomorphous and anomalous differences with PHASES [W. Furey and S. Swaminathan, *Am. Cryst. Assoc. Mtg. Abstr.* **PA33**, 18, 73 (1990)] [overall figure of merit (FOM) = 0.63], produced an initial experimental electron density map with an average amplitude-weighted phase error versus the final refined structure factors (⟨Δφ⟩) of 59.6° and a correlation coefficient between the experimental and final $2F_{obs} - F_{calc}$ maps (R_c) of 0.44. Density modification in DM [K. Cowtan, *Joint Collaborative Computational Project Number 4 (CCP4) and ESF-EACBM Newsletter on Protein Crystallography* **31**, 34 (1994)] under the restraints of solvent flatness, density histogram matching, and Sayre's equation increased the overall FOM to 0.84 and R_c to 0.55 and decreased ⟨Δφ⟩ to 50.9°. Model building into the DM-modified map with XFIT (*40*) produced a model containing 57% of total final scat-

terers (55% of which were fit to sequence and 45% to polyalanine) that was refined by maximum likelihood methods in REFMAC [G. Murshudov *et al.*, *Proceedings of The Daresbury Study Weekend*, p. 157 (1996); CCP4, *Acta Crystallogr.* **D50**, 760 (1994)] (R_{cryst} = 45%, R_{free} = 46%) and used for partial-model, phase-combination with SIGMAA [R. J. Read, *Acta Crystallogr.* **A42**, 140 (1986)] to produce an improved electron density map (R_c = 0.59, $\langle\Delta\phi\rangle$ = 49.5°). Comparison of SIGMAA reduced-bias amplitudes to the measured amplitudes allowed FOM estimates for DM density modification of the partial-model phase-combined map, further increasing R_c to 0.65 and decreasing $\langle\Delta\phi\rangle$ to 40.2°. After cycles of refinement and model building in XFIT and O [T. A. Jones *et al.*, *ibid.* **A47**, 110 (1991)] the resolution was extended to 2.5 Å against a model containing 85% of the final scatterers (R_{cryst} = 38.2%, R_{free} = 43.0%), which was improved by adding water molecules with ARP [V. S. Lamzin and K. S. Wilson, *ibid.* **D49**, 127 (1993)] applied in restrained mode among 50 cycles of recursive REFMAC refinement (on the final cycle R_{cryst} = 28.6%, R_{free} = 36.0%). We completed refinement and resolution extension to 2.1 Å in X-PLOR [A. T. Brünger *et al.*, *Science* **235**, 458 (1987)] using the bulk solvent correction, over cycles of rebuilding to σ_A-weighted $2F_{obs} - F_{calc}$ and $F_{obs} - F_{calc}$ omit electron density maps (Table 1). The mobile loop regions of $iNOS_{ox}$ Δ114 (Fig. 3A) contribute to the refined model but give a high average individual atom isotropic thermal (*B*) value of 45.2 Å^2 (43.5 Å^2 for main-chain atoms, 45.4 Å^2 for side-chain atoms, and 33.7 Å^2 for the imidazole ligands), which agrees with overall *B* estimates from Wilson statistics. Discernible omit electron density and a decrease in R_{free} determined if regions with high *B* values were included in the model.

15. For determining the structure of $P2_12_12_1$-AG, the $P2_12_12_1$-IM model with imidazole and water molecules removed was refined against diffraction data for the isomorphous $P2_12_12_1$-AG crystal by positional refinement in X-PLOR to 2.3 Å resolution. After the entire molecule was rebuilt to omit maps, aminoguanidine was oriented in the active center, refined, and verified by examining $F_{obs} - F_{calc}$ electron density maps. A lower overall *B* value of 37.0 Å^2 (35.8 Å^2 for main-chain atoms, 37.8 Å^2 for side-chain atoms, 32.7 Å^2 for imidazole, and 49.2 Å^2 for aminoguanidine) reflects more overall order in the orthorhombic aminoguanidine complex compared with the imidazole complex.
16. A 2.4 Å resolution $iNOS_{ox}$ Δ114 model, refined in the orthorhombic space group (R_{cryst} = 26.0%, R_{free} = 34.0%), was orientated and fitted in the cubic crystal form by AMoRe [J. Navaza, *Acta Crystallogr.* **A50**, 157 (1994)], giving a correlation coefficient of 0.36 and R_{cryst} = 45.5% against 3.5 Å resolution $P2_13$ diffraction data. Positional refinement to 2.9 Å resolution in REFMAC reduced R_{cryst} to 41.3% and R_{free} to 43.7%. A model of type III *E. coli* CAT refined to 1.75 Å resolution {3cla.pdb [M. R. Gibbs *et al.*, *J. Mol. Biol.* **213**, 167 (1990)]}, 46% identical in sequence to type I CAT, was placed into the type I CAT electron density revealed by σ_A-weighted $2F_{obs} - F_{calc}$ and $F_{obs} - F_{calc}$ electron density maps phased with the $iNOS_{ox}$ refined molecular replacement solution. Simulated annealing in X-PLOR to 2.8 Å resolution decreased R_{cryst} to 26.5% and R_{free} to 32.9%. Cycles of positional refinement, rebuilding to omit electron density maps, and resolution extension to 2.6 Å completed the model (Table 1). Disorder in the CAT molecule resulted in a higher overall *B* value (65.6 Å^2 for main-chain atoms, 69.7 Å^2 for side-chain atoms, 45.1 Å^2 for the imidazole ligands, and 66.6 Å^2 overall) for the refined cubic model than for the orthorhombic models, even though the overall *B* value for $iNOS_{ox}$ is similar in both crystal forms.
17. L. Holm and C. Sander, *J. Mol. Biol.* **233**, 123 (1993).
18. F. C. Bernstein *et al.*, *ibid.* **112**, 535 (1977).
19. M. Sono, D. J. Stuehr, M. Ikeda-Saito, J. H. Dawson, *J. Biol. Chem.* **270**, 19943 (1996).
20. J. C. Salerno, K. McMillan, B. S. S. Masters, *Biochemistry* **35**, 11839 (1996).
21. Q. W. Xie, M. Leung, M. Fuortes, S. Sassa, C. Nathan, *Proc. Natl. Acad. Sci. U.S.A.* **93**, 4891 (1996).
22. J. Wang, D. J. Stuehr, D. L. Rousseau, *Biochemistry* **36**, 4595 (1997).
23. P. F. Chen, A. L. Tsai, V. Berka, K. Wu, *J. Biol. Chem.* **272**, 6114 (1997).
24. R. Gachhui *et al.*, *Biochemistry* **36**, 5097 (1997).
25. D. Mansuy and J. P. Renaud, in (*6*), pp. 537–574.
26. M. Sundaramoorthy, J. Terner, T. L. Poulos, *Structure* **3**, 1367 (1995).
27. N. Sennequier and D. J. Stuehr, *Biochemistry* **35**, 5883 (1996).
28. R. M. Chabin *et al.*, *ibid.*, p. 9567.
29. D. J. Wolff and A. Lubeskie, *Arch. Biochem. Biophys.* **316**, 290 (1995).
30. J. Wang, D. Rousseau, H. M. Abu-Soud, D. J. Stuehr, *Proc. Natl. Acad. Sci. U.S.A.* **91**, 10512 (1994).
31. H. M. Abu-Soud, R. Gachhui, F. M. Raushel, D. J. Stuehr, *J. Biol. Chem.* **271**, 17349 (1997).
32. B. R. Crane *et al.*, data not shown.
33. T. L. Poulos, J. Cupp-Vickery, H. Li, in (*6*), pp. 125–150.
34. M. Wang, D. L. Roberts, R. Paschke, T. M. Shea, B. S. S. Masters, *Proc. Natl. Acad. Sci. U.S.A.* **94**, 8411 (1997).
35. A. D. N. Vaz, S. J. Pernecky, G. M. Raner, M. J. Coon, *ibid.* **93**, 4644 (1996).
36. D. B. Goodin, M. G. Davidson, J. A. Roe, A. G. Mauk, M. Smith, *Biochemistry* **30**, 4953 (1991).
37. L. Vitello, J. Erman, M. Miller, J. Wang, J. Kraut, *ibid.* **32**, 9807 (1993).
38. T. Brittain, R. Blackmore, C. Greenwood, A. J. Thompson, *Eur. J. Biochem.* **209**, 793 (1992).
39. U. Siddhanta *et al.*, *J. Biol. Chem.* **271**, 7309 (1996).
40. D. E. McRee, *J. Mol. Graphics* **10**, 44 (1992).
41. These three NOS structures have excellent stereochemistry with 98.8% of all residues falling in the most favored or otherwise allowed regions of a Ramachandran ϕ/Ψ plot, as defined by PROCHECK [R. A. Laskowski *et al.*, *J. Appl. Crystallogr.* **26**, 283 (1993)]. No residues fall in disallowed regions. Nonbonded contacts were assessed with ERRAT [C. Colovos and T. O. Yeates, *Protein Sci.* **2**, 1511 (1993)] and found to be as likely or more likely than those of a representative group of high-resolution protein structures.
42. We thank C. Mol, C. Putnam, A. Bilwes, and J. Noel for help with data collection, A. Bilwes and D. Goodin for helpful discussions, P. Clark, T. Macke, and J. Zhang for technical assistance, and SSRL for use of data collection facilities. Supported by NIH grants HL58883 and CA53914. D.J.S. is an Established Investigator of the American Heart Association.

20 August 1997; accepted 22 September 1997